

## Research papers

# A multi-scale model for local polarization prediction in flow batteries based on deep neural network

Yansong Luo<sup>a</sup>, Wenrui Lv<sup>a</sup>, Menglian Zheng<sup>a,b,\*</sup>

<sup>a</sup> Institute of Thermal Science and Power Systems, School of Energy Engineering, Zhejiang University, Hangzhou, China

<sup>b</sup> State Key Laboratory of Clean Energy Utilization, School of Energy Engineering, Zhejiang University, Hangzhou, China



## ARTICLE INFO

## Keywords:

Redox flow battery  
Multi-scale model  
Local polarization  
Deep neural network  
Battery management

## ABSTRACT

The side reaction of the flow battery will consume electrons, reduce efficiency, and eventually cause safety problems. Regarding gas management and removal, carefully controlling local over-polarization is a vital issue. However, among the multi-scale models that can predict local polarization, the lack of dimensionality inside the electrode makes it impractical to predict three-dimensional variations. In this work, we propose a three-dimensional multi-scale model that allows the rapid prediction of local polarization, which cooperates with deep neural networks, the pore network model, and the three-dimensional continuum model to have both the advantages of accuracy and extensibility. Parameters such as the porosity, permeability, and specific surface area of the electrode are calculated from 500 randomly generated microstructures, and the training samples for the deep neural network are calculated by the cell-scale model and pore-scale model. Through the developed model, we explore the effects of the interdigitated flow field, variable flow rate optimization strategies, and diverse operating conditions on local polarization. The results show that the proposed model can accurately predict local polarization. The research directions of future work include the collaborative optimization of the electrode's microstructure, the flow field, and the flow rate to ultimately improve the local polarization uniformity.

## 1. Introduction

As the scale of solar energy and wind energy increase dramatically worldwide, the size of energy storage systems is also growing to resolve the contradiction between the discontinuity caused by natural conditions and the continuity of users' demand. Among the energy storage systems, the redox flow battery (RFB) has the advantage of flexible power and energy capacity configurations as well as the fact that its reactants can be made of molecules from a wide range of sources, including metals and organics [1–3]. These advantages ensure that the RFB is cost-effective and becomes one of the critical technologies for large-scale energy storage. Over the last decade, the improvement and development of various components in the battery, including electrodes [4,5], membranes [6–9], bipolar plates [10,11], and electrolytes [12], have been concerned with promoting the battery's performance [13]. The operating conditions [14,15] of the flow battery, including electrolyte flow rate and current density, have also been optimized.

In the field of RFBs, vanadium [16–18], zinc-nickel [19], and iron-chromium [20] flow batteries are all aqueous batteries, facing the risk of side reactions including hydrogen and oxygen evolution. The

formation of bubbles from side reactions reduces the electrochemically active area of the porous electrode, leading to a decrease in energy efficiency. Prolonged hydrogen and oxygen evolution can also lead to the corrosion of the electrodes, thereby shortening the lifetime of the flow battery. Recognizing that the gas side reactions will be exacerbated by high voltage, cut-off voltages are usually set during the charging and discharging processes [21]. Nevertheless, even with preset cut-off voltages, gas side reactions still occur locally due to the heterogeneity of the carbon fibers in the electrode. Owing to the non-uniformity of the microscopic pores of the electrode [22], the electrolyte's velocity and concentration are unevenly distributed at the pore scale, resulting in the lack of reactants and local over-polarization in specific pores. Efforts have been paid to the in-situ imaging for the hydrogen [23] and oxygen evolution reactions [24]; they observed that the hydrogen gas preferred to forming bubbles on the electrode's surface and covering the active sites, while the oxygen evolution corroded the electrode surface. Another method to detect the local polarization of the battery is to establish an electrochemical model. Since the formation of bubbles in the porous electrode occurs at the mesoscopic scale, a pore-scale model [25] is required to describe the mass transfer and polarization of the

\* Corresponding author at: Institute of Thermal Science and Power Systems, School of Energy Engineering, Zhejiang University, Hangzhou, China.

E-mail address: [menglian\\_zheng@zju.edu.cn](mailto:menglian_zheng@zju.edu.cn) (M. Zheng).

local reactants. Qiu et al. [26,27] reported a 3D pore-scale model in which the electrode structures were reconstructed by using X-ray computed tomography (XCT), and the flow of the electrolytes is solved by using the lattice Boltzmann method (LBM). This model examines the local vanadium concentration, overpotential, current density, and overall voltage. Similar models are optimized and widely used in the studies related to electrode material development [28], electrode structure optimization [29], and the investigation of electrode compression ratio [30]. Moreover, the lattice Boltzmann multiphase flow model is applied by Chen et al. [31] to study the evolution of bubble cluster generation by the side reaction. They investigated the effects of porosity, fiber diameter, gas saturation, and solid surface wettability on the coverage of bubbles on the solid surface. The LBM can easily describe the bending boundary and two-phase flow within porous media but requires abounding computing resources with limiting computing regions. Alternatively, approximating the pore structure to a series of ideal spheres and cylindrical channels connecting the spheres, which is called the pore network model method, is an alternative way to build the model. Sadeghi et al. [32] and Lombardo et al. [33] found that the pore network model reduced the simulation time by 4 or 5 times compared with the LBM. Overall, the abovementioned pore-scale models facilitate the understanding of the mass transfer and reaction process within the porous electrode from a subtle perspective, taking into account the influence of electrode's microstructure.

Although the pore-scale models can predict local polarization accurately, the high computational resources and time required by the pore-scale models make it difficult to scale up the pore-scale information towards the whole battery and facilitate the battery design and the battery management in real-world applications. From this point of view, how to scale up the pore-scale model to the entire electrode is the key to the problem. Recently, machine learning has been widely used in economic analysis [34], electrode design [35], and flow field design [36] of RFBs. Bao et al. [37] reported a framework that coupled a deep neural network with a partial differential equation solver and provided an understanding of the relationship between the pore-scale electrode structure reaction and the device-scale electrochemical reaction uniformity. Besides, they proposed a variable flow rate optimization method to promote the surface reaction uniformity.

Alternatively, a variety of operation strategies have been proposed to enhance the mass transfer uniformity within the whole cell. As a common strategy in the battery operation, the flow rate management can effectively improve the energy efficiency of the battery. Most of the proposed strategies concerned the trade-off between the flow battery performance and the energy consumption: increasing the electrolyte flow rate enhances the mass transfer of the active ions to the electrode surface, thereby reducing the concentration polarization; however, the corresponding increment in the pump consumption magnifies the parasitic energy loss of the system. To optimize the flow rate, Ma et al. [38] proposed that stepping up the electrolyte flow rate at the final stage of charging could effectively improve the system efficiency, and Ling et al. [39] applied a pulse electrolyte flow strategy to reduce the pumping cost at a lab-scale flow cell. Although the optimization strategies proposed based on experimental experience were convenient to implement and shown to effectively improve the battery system energy efficiency, accurate and dynamic flow rate optimization strategies called for the support of models. Thus, Kim et al. [40] developed a transient model and investigated the effects of different flow rates on the performance of the flow battery. Tang et al. [41] modeled the concentration overpotential as a function of the flow rate to attain a variable flow rate strategy. It showed that variable flow rates were superior to the constant flow rates, and a flow factor (i.e., the multiple of the theoretical flow rate) of 7.5 was given to obtain overall high system efficiencies for a 40-cell stack. König et al. [42] presented a method to derive the efficiency map according to the operation points and deployed an optimization algorithm to minimize losses in all operation points. Afterward, more factors have been taken into account in the battery performance

prediction models: Fu et al. combined the economic model and the variable flow rate optimization strategy into one model [43]. The concentration discrepancy of the active species in the tank and the stack was factored into the flow rate optimization model developed by Wang et al. [44]. Xiao and Tan [45] proposed a variable flow rate optimization strategy in which the coefficients of the model could be adjusted according to the operating parameters. Yang et al. [46] applied a two-dimensional multi-physical model to analyze the performance of a vanadium redox flow battery under variable operating strategies, based on which they found that the variable flow rate strategy enhanced the overall battery performance compared to that under the constant flow rate strategy.

Although a number of previous studies have developed a series of operation strategies with the help of the cell-scale or the pore-scale models to understand the local polarization, few of them connected the cell-scale and the pore-scale models. Compared to conventional electrochemical models [47], the training data through the machine learning method provide the multi-scale model with the information at the pore scale, with which the local polarization could be ultimately considered in the operation strategies. Furthermore, fewer of them were concerned with the local polarization in the operation strategies. The existing one-dimensional multi-scale model attempted to improve the uniformity of the reaction by controlling the flow rate [37], but it cannot reflect the variations in the other two directions, especially in the through-plane direction. In addition, previous studies based on the deterministic pore reconstruction cannot handle the stochastics of the pore structure subject to a certain pore size distribution, which limits the practical application of the model. In the present study, we propose a solution that allows the operation at the cell scale to adjust the local polarization of the battery into an acceptable range and avoid the occurrence of gas side reactions through the multi-scale model connecting deep neural networks, pore network model, and three-dimensional continuum model. The present work improves the multi-scale model with the novel pore network model, randomly-generated electrode fibers, and extended dimensions to three dimensions, facilitating the study of the electrochemical reaction uniformity and the future work on the design of electrodes and flow fields. The effects of the channel dimensions of the interdigitated flow field and diverse operating conditions on the local polarization distribution are explored. Note that although the proposed framework is based on three specific models, other pore-scale models that are able to predict the local polarization and gas side reaction can also be fitted into the framework to derive different multi-scale models. The rest of the paper proceeds as follows: The framework of the multi-scale model, including the connection among the cell-scale model, the pore-scale model, and deep neural networks, is presented in Section 2. The results of the multi-scale model and predictions for the local polarization under varying flow rates, concentrations of the reactants at the inlet, voltages, and porous medium are presented in Section 3. And Section 4 concludes the paper.

## 2. Methods

To rapidly predict the local polarization on the surface of the electrode, a multi-scale model that connects the cell-scale and pore-scale models is developed, as shown in Fig. 1. The pore-scale model is developed based on the pore network method and used to predict the effects of various microstructures on the electrode permeability, specific surface area, and electrochemical reaction. In contrast, the cell-scale model can simulate the flow of electrolytes and the mass transfer of the reactants inside the whole electrode, but the continuum model neglects the effects of the electrode's microstructure. The contradiction between the two models necessitates the development of the multi-scale model. The deep neural network model acts as a bridge in the framework, which proceeds as follows: (1) The pore network model is developed with diverse microstructures (i.e., pore network) being used as inputs to obtain a large amount of local polarization data under

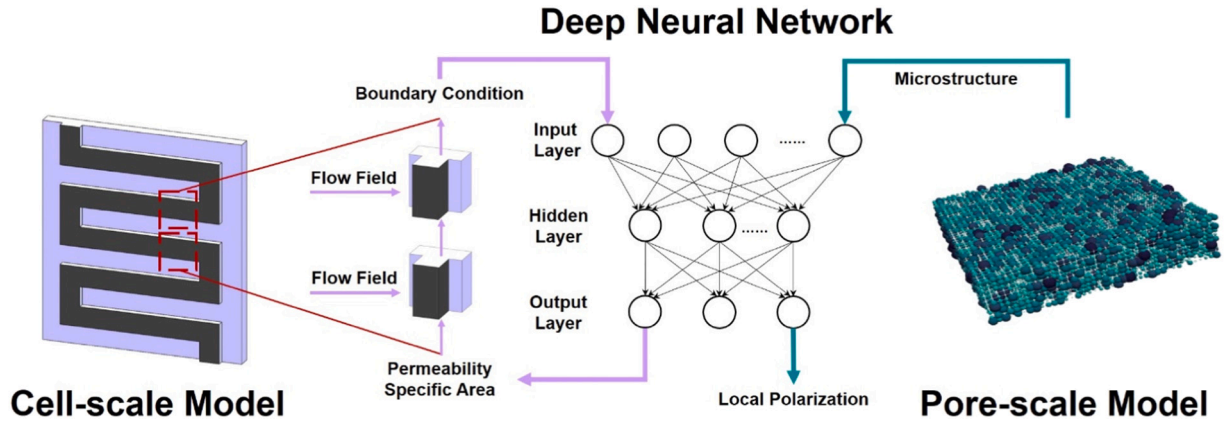


Fig. 1. Framework of multi-scale model for local polarization prediction and flow rate optimization.

varying initial and microstructure conditions. (2) The deep neural network is trained based on the local polarization data which are labeled by the characteristic values of the flow rate, reactant concentration, voltage, and microstructure. (3) The cell-scale model is then developed to calculate the electrolyte's flow, concentration, and potential distribution under specific flow fields and operating conditions for several regions, the results of which are used in the deep neural network model to quickly predict local polarization in each region.

In this paper, as an example, the multi-scale model is devised for the positive half cell of a vanadium redox flow battery. The parameters for this case are provided in Table 1. It should be noted that both the simulations and the experiments are based on the galvanostatic charge and discharge. The cell-scale model for the whole cell, the pore-scale model for the positive half-cell, and the deep neural network for the positive half-cell are demonstrated in Sections 2.1, 2.2, and 2.3, respectively. Moreover, the models are validated by the experimental results in Section 2.4.

### 2.1. Cell-scale model

A three-dimensional, multi-physical, cell-scale model is developed in COMSOL Multiphysics® to calculate the electrolyte's velocity, reactant concentration, and potential distribution. These distributions are used as boundary conditions for the pore-scale model to obtain local

polarization further. It should be noted that interdigitated flow field is applied in the cell-scale and pore-scale models to ensure simulation synchronization.

In this model, it is assumed that:

- (1) Temperature effects are regarded as negligible [49];
- (2) The fluids are considered incompressible [50];
- (3) The side reactions are assumed to be negligible [51];
- (4) The crossovers of vanadium ions and water are ignored [51].

#### 2.1.1. Velocity distribution

The Free and Porous Media module in COMSOL Multiphysics® describes the electrolyte flow in the channel and porous electrode. In detail, the Navier-Stokes equation to model the fluid flow in interdigitated channels and the Brinkman equation for the porous electrode are employed [52]. These equations are shown in Eqs. (1) and (2):

$$\nabla \cdot u = 0 \quad (1)$$

$$\rho(u \cdot \nabla)u = \nabla \cdot [-pI + \mu(\nabla u + (\nabla u)^T)] \quad (2)$$

$$\frac{\rho}{\varepsilon}(u \cdot \nabla) \frac{u}{\varepsilon} = \nabla \cdot \left[ -pI + \frac{\mu}{\varepsilon}(\nabla u + (\nabla u)^T) \right] - \frac{2\mu}{3\varepsilon} \nabla(\nabla \cdot u) - \frac{\mu}{\kappa} u \quad (3)$$

where  $\rho$  denotes the fluid density,  $u$  denotes the fluid velocity,  $p$  denotes the pressure,  $I$  denotes the identity matrix,  $\mu$  denotes the dynamic viscosity,  $\varepsilon$  denotes the porosity, and  $\kappa$  denotes the permeability.

#### 2.1.2. Concentration distribution

The concentration of ions in the electrolyte is handled based on mass conservation, which can be expressed as Eq. (3):

$$\nabla \cdot N_i = -S_i \quad (4)$$

where  $N_i$  denotes the flux of the species,  $S_i$  denotes the source term. The flux of the species can be calculated by the Nernst-Planck equation [53]:

$$N_i = -D_i^{eff} \nabla c_i - z_i u_i^{eff} c_i F \nabla \phi_e + u c_i \quad (5)$$

where  $c_i$  denotes the concentration of species  $i$ ,  $F$  denotes the Faradaic constant,  $z_i$  denotes the ion valence,  $\phi_e$  denotes the ionic potential,  $D_i^{eff} = \varepsilon^{1.5} D_i$  and  $u_i^{eff} = \varepsilon^{1.5} u_i$  denote the effective diffusivity and effective diffusivity of species  $i$ , respectively.

#### 2.1.3. Potential distribution

The charge conservation can be expressed as Eq. (6):

$$\nabla \cdot i_e = -\nabla \cdot i_s = j \quad (6)$$

Table 1  
Parameters and properties in the model.

Description	Symbol	Value	Units
Density of electrolyte	$\rho$	1000 [26]	kg/m <sup>3</sup>
Viscosity of electrolyte	$\mu$	$1 \times 10^{-3}$ [26]	Pa·s
Porosity of electrode	$\varepsilon$	From neural network	/
Permeability of electrode	$\kappa$	From neural network	m <sup>2</sup>
Specific surface area of electrode	$a$	From neural network	m <sup>-1</sup>
Diffusion coefficient of V <sup>4+</sup>	$D_{V_4}$	$3.9 \times 10^{-10}$ [48]	m <sup>2</sup> /s
Diffusion coefficient of V <sup>5+</sup>	$D_{V_5}$	$3.9 \times 10^{-10}$ [48]	m <sup>2</sup> /s
Number of electrons	$z$	1	/
Standard reaction rate constant	$k$	$6.8 \times 10^{-7}$ [48]	m/s
Transfer coefficient	$\alpha$	0.5	/
Standard reaction potential of positive reaction	$E_0$	1.004 [48]	V
Operating temperature	$T$	298.15	K
Conductivity of membrane	$\sigma_m$	10 [10]	S/m
Conductivity of electrode	$\sigma_e$	1000 [10]	S/m
Conductivity of current collector	$\sigma_c$	1000 [10]	S/m
Thickness of electrode	$w_e$	0.0005	m
Cross-section area of inlet channel	$A$	$1 \times 10^{-6}$	m <sup>2</sup>
Initial concentration of vanadium species	$c_0$	1600	mol/m <sup>3</sup>

where  $j$  denotes the local current density,  $i_e$  and  $i_s$  denote the ionic current density and electronic current density, respectively, according to Faraday's law and Ohm's law [54], which can be calculated as:

$$\vec{i}_e = F \sum_i z_i \vec{N}_i \quad (7)$$

$$\vec{i}_s = -(1 - \varepsilon)^{1.5} \sigma_s \nabla \phi_s \quad (8)$$

where  $\phi_s$  denotes the electronic potential in the solid phase and  $\sigma_s$  denotes the electronic conductivity. The local current density is formulated by the Butler-Volmer equation [55] as follows:

$$j = a F k c_O^{(1-\alpha)} c_R^\alpha \left[ \frac{c_O^s}{c_O} \exp\left(-\alpha \frac{F}{RT} (\phi_s - \phi_e - E_{eq})\right) - \frac{c_R^s}{c_R} \exp\left((1-\alpha) \frac{F}{RT} (\phi_s - \phi_e - E_{eq})\right) \right] \quad (9)$$

where  $a$  denotes the specific surface area,  $k$  denotes the reaction rate constant,  $\alpha$  denotes the charge transfer coefficient, the subscripts  $O$  and  $R$  denote oxidation and reduction, respectively, and the superscript  $s$  denotes the electrode surface and  $E_{eq}$  denotes the equilibrium potential, which can be expressed as:

$$E_{eq} = E_0 + \frac{RT}{F} \ln\left(\frac{c_O}{c_R}\right) \quad (10)$$

where  $E_0$  denotes the standard equilibrium potential for the redox couple.

In Eq. (8), the term  $c_i^s$  denotes the concentration of species  $i$  at the electrode surface, which can be calculated from the balance of the electrochemical reaction rate and the reactant's mass transfer rate as [11]:

$$k_m (c_i - c_i^s) = F k c_O^{(1-\alpha)} c_R^\alpha \left[ \frac{c_O^s}{c_O} \exp\left(-\alpha \frac{F}{RT} (\phi_s - \phi_e - E_{eq})\right) - \frac{c_R^s}{c_R} \exp\left((1-\alpha) \frac{F}{RT} (\phi_s - \phi_e - E_{eq})\right) \right] \quad (11)$$

where  $k_m$  denotes the mass transfer coefficient.

To fundamentally satisfy the active species requirement in the electrode, the flow rate must reach the minimum level varying with the state of charge (SoC), which can be calculated as follows [44]:

$$Q_{\min} = \begin{cases} \frac{|I|}{F \times c \times \text{SoC}}, \text{discharge} & \text{(a)} \\ \frac{|I|}{F \times c \times (1 - \text{SoC})}, \text{charge} & \text{(b)} \end{cases} \quad (12)$$

where  $c$  denotes the concentration of active species, and  $\text{SoC}$  denotes the state of charge. However, considering the diffusion layer near the surface of the electrode, a multiplying factor  $f_c$  is employed to decrease the concentration overpotential. So, the final flow rate is expressed as:

$$Q = f_c \times Q_{\min} \quad (13)$$

#### 2.1.4. Boundary conditions

The velocity and pressure conditions at the inlet and outlet of the channel are given, respectively:

$$u_{in} = Q/A \quad (14)$$

$$p_{out} = 0 \quad (15)$$

where  $A$  denotes the cross-section area of the inlet channel. The other boundaries of the channel and electrode are set with no-slip boundary conditions.

The inlet concentrations of vanadium species are defined with the given SoC:

$$c_{V^{2+}}^{in} = c_0 \cdot \text{SoC} \quad (16)$$

$$c_{V^{3+}}^{in} = c_0 \cdot (1 - \text{SoC}) \quad (17)$$

where  $c_0$  denotes the initial value of the vanadium concentration. And at the outlet of the channel, the reactant diffusive fluxes are set to zero:

$$-D_i^{eff} \nabla c_i = 0 \quad (18)$$

The other surfaces of the electrode and channel are set with no flux boundary, i.e.,  $N_i = 0$ .

The flux conditions for the potential distribution of the electrode along the collector interface and the electrolyte along the membrane interface are written as follows [56]:

$$-\sigma_c \nabla \phi_s = -I \quad (19)$$

$$-\sigma_m \nabla \phi_l = I \quad (20)$$

where  $I$  denotes the applied current density. Zero charge flux conditions are applied for other surfaces of the collector, electrode, and membrane.

More details of the model and relevant parameters in this paper can be found in our previous literature [10], and the geometric parameters for the specific battery configuration are provided in Supplementary material. It is worth mentioning that in the cell-scale model, the electrode area is 3.24 cm<sup>2</sup>, divided into 81 square regions to respond to the modeling area of 4 mm<sup>2</sup> in the pore-scale model.

## 2.2. Pore-scale model

The pore network model, which has been demonstrated to reduce the simulation resources compared to the LBM, is developed in this work to investigate the local polarization distribution at the pore scale. The model is basically under the assumption that:

- (1) Intensive properties such as pressure and concentration vary slightly within each pore;
- (2) The electrolyte is a dilute solution;
- (3) The reaction only occurs inside the pores but not throughout the throats [57].

### 2.2.1. Geometric modeling

The pore network model consists of spheroids and cylinders: on the one hand, spheroids represent the void space of the porous medium where electrochemical reactions occur; on the other hand, the cylinders connect two spheroids as a throat where the fluid flows through. Compared with the finite element method or the finite volume method, the pore network model enables larger porous domains. In this work, the modeling domain is a cube with a 4 mm<sup>2</sup> cross-section area and 0.5 mm thickness, where 32, 32, and 8 grid points are set in each direction, respectively. Since the deformation effect [58] of the electrode can play an important role in battery prediction results, the pore size distribution of compressed SGL 25AA [59] is employed in the model to generate a pore network. To quickly simulate the complex and disordered structure of the carbon-felt-based electrode, the pore network generates randomly satisfying the condition that the sum of adjacent pore radius is less than the length of the throat. Then a reasonable pore network is generated and added to the dataset in the deep neural network model as shown in Section 2.3. More details can be found in Supplementary material.

### 2.2.2. Mathematical modeling

The governing equations involved in the pore-scale model are mostly the same as those in the cell-scale model, except for two equations. One is the equation for mass conservation:

$$-\sum_{j=1}^{n_i} \rho u_{ij} A_{ij} = 0 \quad (21)$$

where  $n_i$  denotes the number of neighbor pores to pore  $i$ ,  $u_i$  denotes the fluid velocity from pore  $i$  to pore  $j$ , and  $A_{ij}$  denotes the cross-section area of the connecting throat. To accurately describe the velocity between pores, the Hagen-Poiseuille equation is defined as:

$$u_{ij} = \beta_{ij} (p_i - p_j) \quad (22)$$

where  $p_i$  and  $p_j$  denote the pressure of pore  $i$  and pore  $j$ , respectively, and  $\beta_{ij} = S_{ij}/8\pi\mu l_{ij}$  denotes the hydraulic conductance of the throat of length  $l_{ij}$ . Another equation is the conservation of species:

$$-\sum_{j=1}^{n_i} m_{ij} A_{ij} = R_i \quad (23)$$

where  $R_i$  is the net reaction rate in pore  $i$ , and  $m_{ij}$  denotes the mass flux from pore  $i$  to pore  $j$ , which is expressed by the following equation [57]:

$$m_{ij} = u_{ij} \left( c_i + \frac{c_i - c_j}{\exp\left(\frac{u_{ij} l_{ij}}{D}\right) - 1} \right) \quad (24)$$

where  $c_i$  and  $c_j$  denote the concentrations of species in pore  $i$  and pore  $j$ , respectively, and  $D$  denotes the hydraulic diameter of throats. The local reaction rate in the pore can indicate how local polarization occurs, Thereby, the parameter  $R_i$  is used to represent the severity of local polarization, which is also an output variable in the deep neural network model.

### 2.2.3. Boundary conditions

In the pore-scale model, most of the boundary conditions are set the same as in the cell-scale model, except that the inlet of the electrolyte is moved above the electrodes, as shown in Appendix. In addition to this, unlike uniform current density at the cell scale, the potential distribution of the pore-scale model is the calculated local voltage:

$$\phi_s = V_{local} \quad (25)$$

### 2.3. Deep neural network model

The fiber weaves within carbon felt, leading to a complicated structure at different locations in the same electrode. By interacting with the varying flow and concentration fields, the microstructure can entail the unexpected occurrence of local over-polarization. Considering various microstructures in models are necessary to thoroughly explore the local polarization, which brings about large computing consumption, this work introduces deep neural networks (DNN) to quickly predict the local polarization with diverse microstructures.

When the reaction rate decreases, it indicates that the local reactant is insufficient, which will cause over-polarization and may lead to gas side reactions. Thus, the local reaction rate is considered one of the output variables of the DNN model. In addition, macroscopic parameters, including porosity and permeability of the porous media and specific surface area, are also important outputs. Regarding the inputs, voltage, the concentration of species, the flow rate of the electrolyte, and characteristics of the microstructures are determined to be input variables for learning complex local polarization. Since the electrolyte flow path is affected by the pore size and distribution, this work sets the sum of the product of the pore diameter  $d_{pi}$  and the coordinates of the grid

$[x_i, y_i, z_i]$  where pore  $i$  is located as the input variable  $[X, Y, Z] =$

$\left[ \sum_i d_{pi} x_i, \sum_i d_{pi} y_i, \sum_i d_{pi} z_i \right]$  to characterize diverse microstructures.

Specifically, five hundred pore networks with the same probability

density function (pore size distribution from SGL 25AA) were generated for preparing machine learning data. The input variables  $X$ ,  $Y$ , and  $Z$  are calculated based on the generated microstructures. In addition, boundary conditions for the pore-scale model, including electrolyte velocity, concentration, and voltage, are taken into the dataset, as shown in Table 2. The machine learning of this work is divided into two parts: the first part is based on the input variables  $X$ ,  $Y$ , and  $Z$ , employing 500 different pore networks as a database to learn the macro parameters of porosity, permeability, and specific surface area, which will be substituted into the cell-scale model to obtain the multi-physical field; the second part is based on the calculated multi-physical field, taking ten types of input voltage, ten types of inlet electrolyte concentration, ten types of inlet flow rate as input variables, supplemented by a combination of 10 randomly selected pore networks to form a database of 10,000 data to learn local polarization under diverse operating conditions and microstructures. The Python package Pytorch establishes the DNN model in this study. In short, the employment of DNN aims to simplify the computation of the pore-scale model and to achieve rapid and accurate prediction of local polarization.

### 2.4. Model validation

Experiments have been implemented to validate the cell-scale model and the pore-scale model. For the flow cell, the electrode was a  $5 \times 5$  cm<sup>2</sup> graphite felt (SGL®, GFA5) with the thermal treatment at a rate of 5 °C/min to 400 °C for 12 h. The diameter of the graphite felt fibers was measured by scanning electron microscopy, while the porosity and the specific surface area were measured through the Brunauer Emmett Teller method. The electrolytes (1.6 M vanadium in 4 M sulfuric acid) were circulated by the peristaltic pumps (Masterflex®, L/S 07525-40) at a flow rate ranging from 10 to 20 mL/min. The galvanostatic charge and discharge tests were conducted at the current density corresponding to 40 mA/cm<sup>2</sup> with the upper and lower voltage being set as 1.8 and 0.8 V, respectively, by the workstation Bio-logic® VSP. The positive and negative tanks' electrolyte volumes were set as 30 mL. The nitrogen was aerated to the negative tank to avoid the oxidation of the negative species, and the experiments were conducted under a constant room temperature corresponding to 25 °C. As shown in Fig. 2(a), the results show that when the flow rate increases from 10 mL/min to 20 mL/min, the cell-scale model is in good agreement with the experimental results, with a maximum error of 0.5 %, which may be due to the ignorance of the side reactions and crossover in the model.

The polarization curve and power density curve obtained by using the pore-scale model are compared with the experimental results obtained by using the above-mentioned flow cell setups (the applied flow rate is 10 mL/min), and the results show that the model has an excellent agreement at high current densities, while the error at low current

**Table 2**  
Description and values of input or output variables.

Input or output variable	Description	Values
X	Distribution of pores in x-direction	Calculated based on selected microstructure
Y	Distribution of pores in y-direction	
Z	Distribution of pores in z-direction	
E	Input voltage (V)	0.1, 0.2, 0.3, ..., 1.0
C	Inlet concentration of reactant (mol/m <sup>3</sup> )	300, 400, 500, ..., 1200
Q	Inlet flow rate of electrolyte (mL/min)	2, 4, 6, ..., 20
$\epsilon$	Electrode porosity	Predicted according to specific pore network
$\alpha$	Specific surface area	
$\kappa$	Hydraulic permeability	
$R_i$	Local reaction rate	Predicted

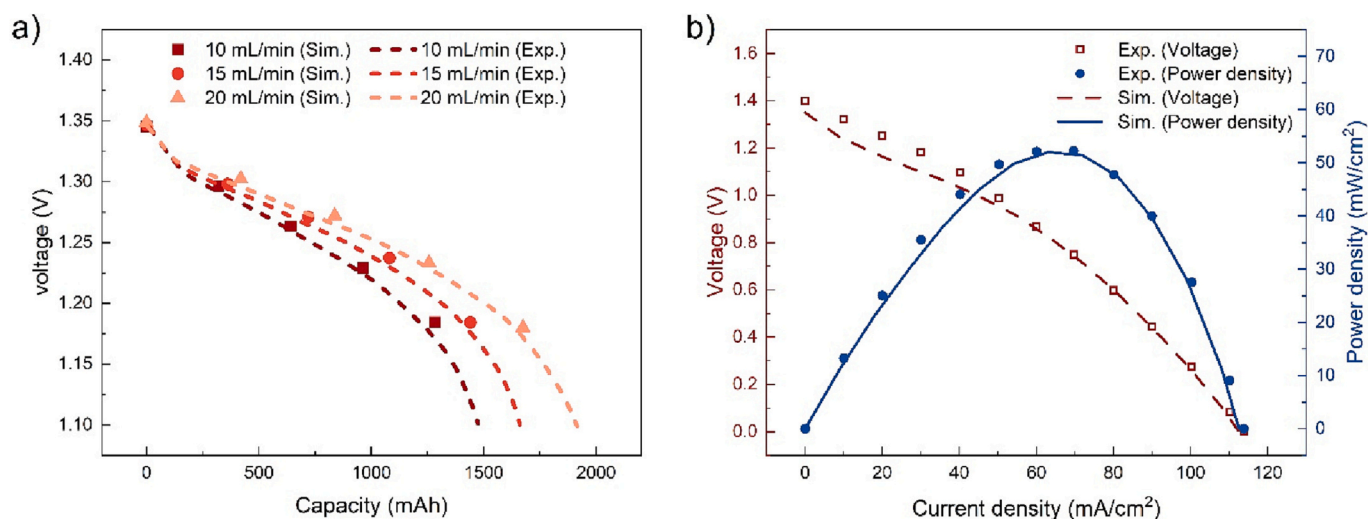


**Fig. 2.** (a) Validation of cell-scale model compared to experimental results with discharging under the flow rate corresponding to 10, 15, and 20 mL/min. (b) Polarization curve and power density curve obtained by using pore-scale model and experimental results. The applied flow rate was 10 mL/min. Sim. and Exp. are short for simulative and experimental results, respectively.

densities is about 3.9%. At low current densities, voltage losses mainly consist of activation polarization. The reason for the relatively large deviation in the simulation results at low current densities may be attributable to the pore network model that uses spheres and cylinders to simulate the microstructure of the porous electrode. Such approximation underestimates the specific surface area of the electrode, and then the overall reaction area decreases. Last but not least, this model can complete steady-state calculations within 3 min on a computer with the AMD® EPYC® 7452 CPU.

### 2.5. Computational superiority

Compared with the previous multi-scale model [37], the present study utilizes the pore network model in place of the LBM method. As mentioned in the literature [33], the computational time of the pore network model is reduced by 4–5 times that of the LBM method. In this manner, the dimension of the model can be extended to three dimensions at relatively small computational expenses. In addition, through the deep neural network, the outputs from the pore-scale model such as permeability and specific area which are dependent on the electrode's microstructure are quickly predicted, largely reducing the computational time required to connect the cell-scale model and the pore-scale model.

## 3. Results and discussion

### 3.1. Reaction rate distribution at pore scale

In this study, the pore-scale model is employed to calculate the distribution of the local reaction rate of reactants, denoting the local polarization distribution as Fig. 3 shows. The area with a high ion reaction rate in the figure is highlighted in yellow, representing that the reactants here are sufficient and the polarization overpotential is relatively low. In contrast, the area with low ion reaction rates is marked in violet, representing that the reaction here is limited by mass transfer and the polarization overpotential is high. To further explore the effects of different operating conditions on the local reaction rate, different flow rates, concentrations, and voltages are applied to the boundary conditions of the electrodes, as shown in Fig. 3. We find that even preferred conditions (such as Fig. 3(b), (d), (f)) cannot eliminate the low reaction rate regions, especially near the outlet. As shown in Fig. 3(a) and (b), when the flow rate into the electrode increases from 5 to 15 mL/min, the regions with high local reaction rate increases from about 20% to 80%, gradually propagating from the electrolyte inlet to the outlet, indicating that the increment of the flow rate effectively improves the local mass transfer of the reactants. With the increment of flow rates, the region of high reaction rate flipped from the side near the inlet to the other side.

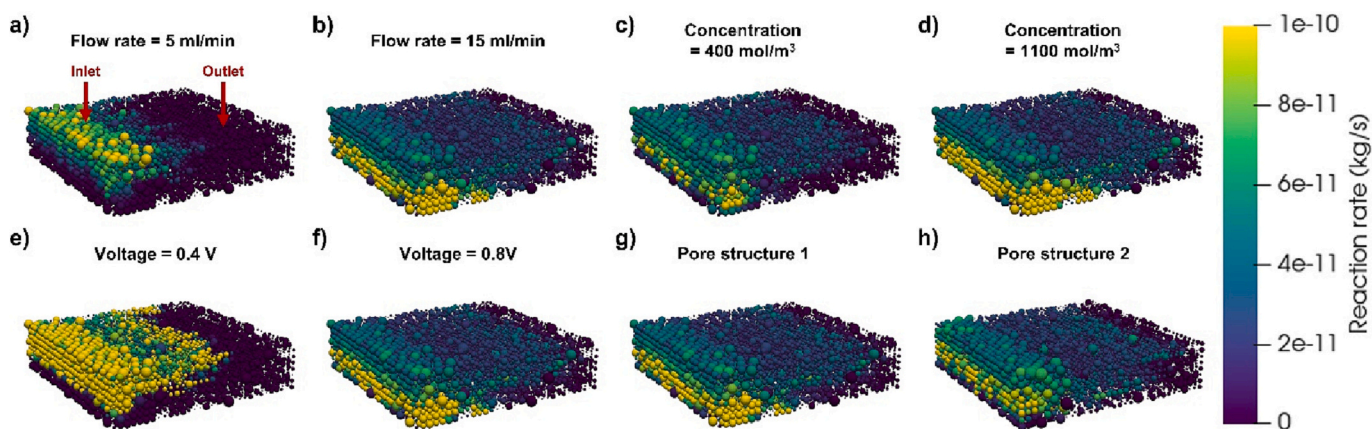


**Fig. 3.** Reaction rate distribution of vanadium pentavalent ion in the pore-scale model under (a) 5 mL/min, (b) 15 mL/min, (c) 400 mol/m<sup>3</sup>, (d) 1100 mol/m<sup>3</sup>, (e) voltage = 0.4 V, (f) voltage = 0.8 V, and (g) one kind of pore network, (h) another kind of pore network.

According to the Butler-Volmer equation, the reaction rate is dependent on the overpotentials as well as the concentration of the reactants (Eq. (9)). When the applied flow rate is relatively low, the reaction is limited by the mass transfer of the reactants towards the surface of the carbon fibers, and thereby the region near the inlet, where the concentration of the reactants is relatively high, shows high reaction rates. With a substantial increment in the applied flow rate (e.g., from 5 mL/min to 15 mL/min as shown in Fig. 3), the distribution of the reaction rate is less constrained by the mass transfer of the reactants. Rather, the distribution of the overpotential plays an important role. Since the direction of the current is from the boundary of the bipolar plate to the boundary of the membrane, the potential difference will rise in this direction. Thus, the overpotential near the membrane will be larger, resulting in a higher reaction rate on the side near the membrane. This phenomenon was also observed in the previous studies that the reaction rate is higher near the membrane than that near the bipolar plate (e.g., [57]). The average reaction rate of the whole electrode at the high flow rate is 2.9 times that at the low flow rate.

A similar situation is also observed in the cases of variations in the concentration and voltage as Fig. 4(c)–(f) show. When the concentration at the inlet increases from 400 to 1100 mol/m<sup>3</sup> and the voltage increases from 0.4 to 0.8 V, more pores with high reaction rates appear, indicating that the operating conditions affect the local polarization significantly. The average reaction rate of the whole electrode at the high concentration and the high voltage are 1.9 folds and 1.4 folds, respectively, those at the low concentration and the low voltage. In addition, microstructures also cause differences in the internal mass transfer within the electrode, as shown in Fig. 4(g) and (h): two diverse microstructures entail the reaction rate distribution inside the electrode discrepant.

The results show that in addition to the operating conditions, the microstructure of the electrode also causes differences in the distribution of local polarization. When developing the multi-scale model, the diversity of microstructures needs to be taken into account. In order to factor the impacts of the velocity, concentration, voltage, and microstructure into the multi-scale model, DNN is integrated into the framework relying on the large amount of data produced by the pore-scale

model. The following subsections will display the quick prediction results through the DNN model.

### 3.2. Prediction of deep neural networks

DNN is a widely employed deep learning framework based on artificial neural networks with multiple hidden layers. In this study, the DNN fills the gap between the macroscopic parameters and local polarization that varies with the microstructure, making it possible to optimize the local polarization by adjusting the macroscopic parameters. For the DNN prediction, the dataset includes 500 pore networks based on the pore diameter distribution curve of compressed carbon felt (see Supplementary material) and 10,000 samples with varying operation conditions. The dataset is then split into three subsets, including the training set occupying 50 % of data to train weighting parameters, the validation set occupying 30 % of data to determine the layer structures and hyperparameters, and the test set occupying 20 % of data to evaluate the model performance. In this study, the hidden layers for each layer are all set with 400 neural nodes, respectively.

The prediction performance of DNN is shown in Fig. 4, showing good agreements between the predicted and the test data. However, some discrepancies are observed in the specific surface area and the porosity, which may be caused by the generation process for the pore network. When the pore network is generated based on the pore size distribution curve, due to the limitation that the diameter of adjacent pores cannot exceed the mesh's length (Supplementary material), resulting in the random generation of pore networks that are conformed to a particular porosity and specific surface area. Moreover, it should be noted that the local reaction rate dependent on the six input variables shows a good fitting, and the mean-squared error of the model is  $1.5 \times 10^{-3}$  after 1000 epochs of training.

Good fits of the parameters and local polarization show that the variables used in this study can appropriately describe the changes brought by diverse microstructures and operating conditions. Additionally, the designed neural network structure is also effective. The accurate prediction of the DNN model is a key part of the multi-scale

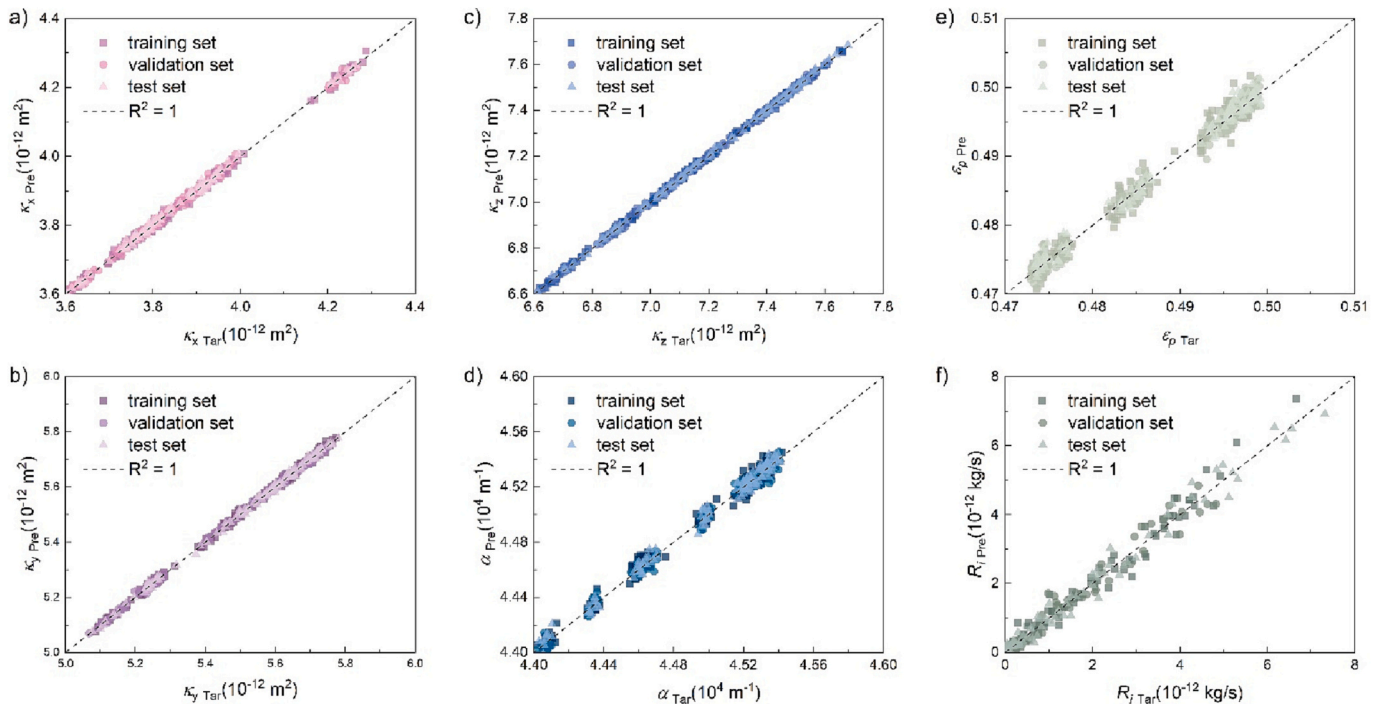


Fig. 4. Agreements between predicted permeability through deep neural networks (subscript “Pre”) and targeted permeability obtained by using pore-scale model (subscript “Tar”): (a) in x-direction, (b) in y-direction, and (c) in z-direction. Comparisons between predicted and targeted values: (d) specific surface area, (e) porosity, and (f) local reaction rate.

model, which enables the DNN to accept the input of the cell-scale model and output the local polarization instead of the pore-scale model, so as to predict the local polarization at the cell scale.

### 3.3. Reaction rate distribution at cell scale

We further explore the effects of diverse operating conditions on the distribution of the reaction rate at the cell scale. As shown in Fig. 5(a), when the flow coefficient  $f_c$  increases from 2 to 10, the local reaction rate of vanadium pentavalent ion gradually grows, and the average reaction rate of the entire flow cell is increased by 2.4 times. From the distribution map, low reaction rate areas are still observed. The distribution of the reaction rate under varying velocity, concentration, and voltage of the electrolyte is investigated, as shown in Fig. 5(b)–(d). Owing to the interdigitated flow field, the electrolyte flows faster under the ribs, represented by the red regions in Fig. 5(b). Furthermore, the relatively large pores in the porous electrode lead to preferred paths and flow “dead zones”, which have been confirmed by several previous studies [22,60]. Owing to the effects of the inhomogeneous distribution of the pores and the flow field, increasing the flow rate can improve the overall polarization distribution, but cannot eliminate the over-polarization on the electrode surface completely.

In addition, the effects of current densities and SoCs on the local reaction rate of the vanadium pentavalent ion ions are investigated in this study. As shown in Fig. 6, the overall distribution of the local reaction rates follows similar trends, which are largely affected by the differences in the under-the-rib and the under-the-channel electrolyte velocities (see Fig. 5). The discrepancies are likely associated with the randomly generated pore networks in different cases. Additionally, it should be noted that although the flow factor (determined by the SoC, applied current density, and flow rate; see Eqs. (15), (16)) keeps the same in all the investigated cases in Fig. 6, the local reaction rate shows the distinct distribution in the flow cell. Existing flow strategies are typically adjusted according to the SoC and the applied current density, ignoring the inhomogeneity caused by the flow field and microstructure. Thus, future flow rate optimization strategies need to consider more factors including the synergy of operating conditions, flow field, and electrode microstructure to control local over-polarization.

Nevertheless, the microstructure of the carbon-based electrode material should be further improved along with the novel flow fields to alleviate the pore-scale and cell-scale flow “dead zones”, which can hardly be addressed by the flow rate management.

### 3.4. Future work

This paper proposes a method that can quickly predict local polarization; however, further adjustment methods for alleviating the local over-polarization are not fully proposed. Although adjusting the flow rate can reduce the polarization to a certain degree, the local polarization remains too low in the dead flow zones affected by the flow field and the microstructure of the electrode. To this end, to thoroughly avoid local over-polarization, the ultimate solution is the simultaneous optimization of the flow field and electrode’s microstructure designs as well as the applied flow rate through advanced machine learning and additive manufacturing methods such as 3D printing, and thereby substantially enhancing the uniformity of the electrolyte flow in the porous electrode. Wan et al. [35] developed a coupled machine learning and genetic algorithm framework to effectively optimize the arrangements and diameters of carbon fibers for simultaneously optimizing the specific surface area and the hydraulic permeability of the electrode, which is expected to be extended to include the local polarization objective for optimization in the future. In addition, the proposed battery management strategy can also influence the distribution of the two-phase flow in the porous medium composed of aqueous electrolytes and bubbles generated by side reactions. Thus, a two-phase flow model should be added to the framework in the hope that gas management and removal at multiple scales can be achieved.

For real-time operation, some parameters, especially those that vary with the degradation process, should be in-situ, real-time measured, and updated in the model during the cycling process. And the potential solution is to utilize advanced in-situ measurement technologies and prepare more real-world data for training. To be specific, in real-time operation, the proposed model requires real-time measurements for the parameters including flow rate, inlet reactant concentration or state of charge, and voltage of the battery system, and then calculates the local polarization based on these parameters. Additional parameters

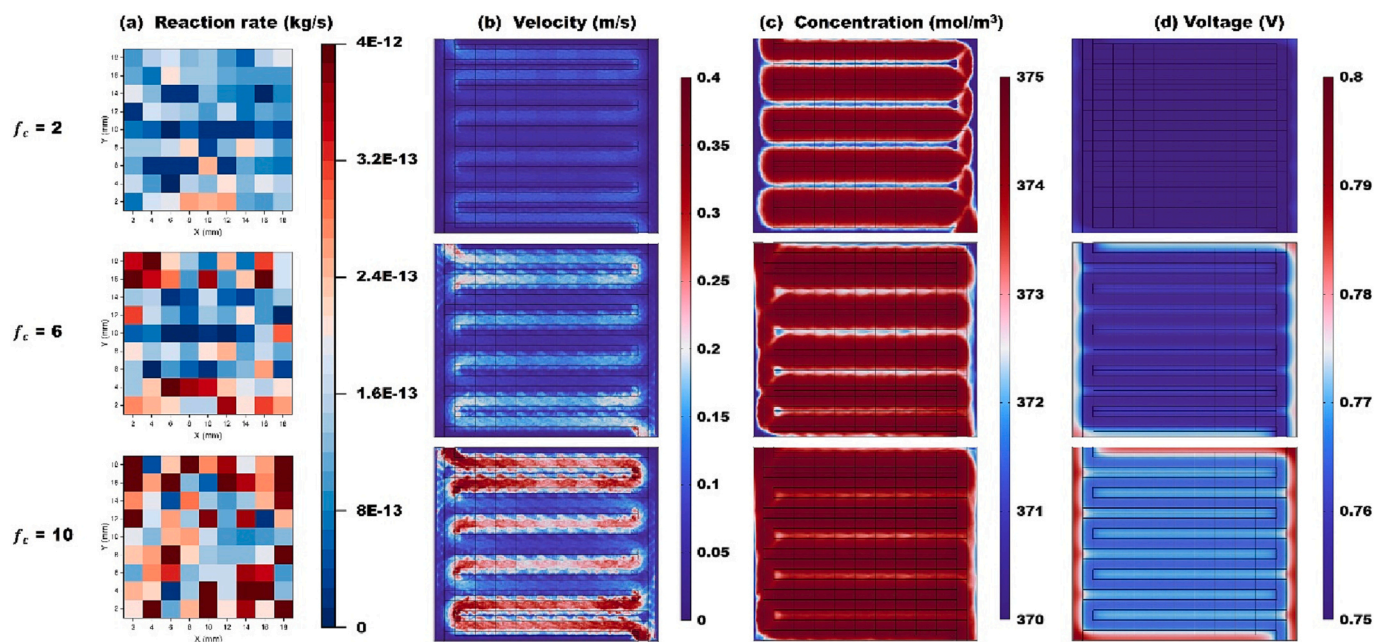


Fig. 5. (a) Predicted local reaction rate distribution through multi-scale model under varying electrolyte flow rates, and distributions of (b) velocity, (c) concentration of vanadium pentavalent ion, and (d) voltage simulated by cell-scale model. Results are at the central section of the electrode and under  $300 \text{ mA/cm}^2$  current density and SoC corresponding to 0.25. The flow coefficient  $f_c$  varies at 2, 6, and 10.

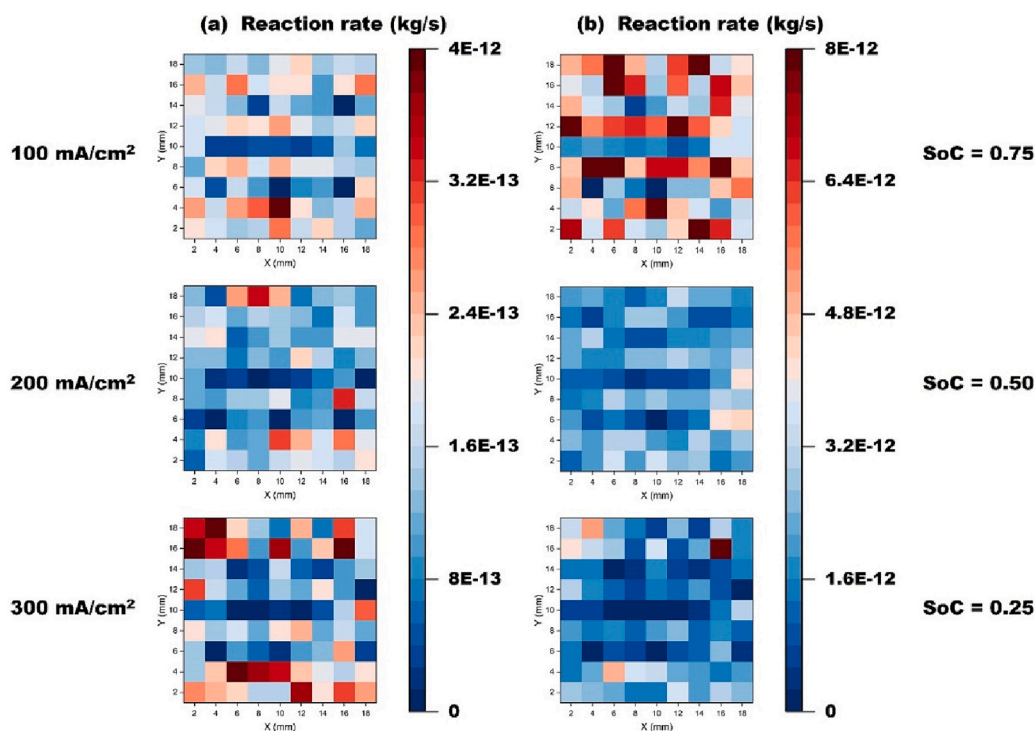


Fig. 6. Predicted local reaction rate distribution through multi-scale model under (a) varying applied current densities ( $SoC = 0.25, f_c = 6$ ) and (b) varying SoCs ( $300 \text{ mA/cm}^2, f_c = 6$ ).

required for the model, including the physical properties of the electrode and the electrolyte, and the standard values of the electrochemical reaction kinetics, do not change during operation. Nevertheless, considering degradation, the abovementioned properties of the electrode and the electrolyte may also change. For example, the concentration of the reactants may be influenced by crossover and gas side reactions, bringing variations in the properties of the electrolyte such as conductivity and viscosity. To this end, in real-world systems, more electrode pore structures and operating parameters may skew the predictions of deep neural networks and should be considered during the training process in the future.

#### 4. Conclusions

The present paper proposes a multi-scale model that can quickly predict the local polarization of the RFBs, which combines the pore-scale model, the deep neural network, and the cell-scale model. Some main findings and contributions of the present study are as follows:

- (1) A multi-scale model incorporating both electrode's microstructure and the flow field was constructed, based on which the operating strategy for alleviating local over-polarization and the future's simultaneous optimization for the flow field and microstructure could be implemented. The microstructures were randomly generated in different areas of the electrode and subject to a given pore size distribution, to represent the stochastic and the pore structure characteristic of the electrode.
- (2) By using the developed multi-scale model, the impacts of the interdigitated flow field with various operating conditions and electrode microstructures on the local reaction rate distribution were extensively explored. With the interdigitated flow field, the local polarization inside the electrode will be affected by the electrolyte velocity, concentration, and electric potential field. When the flow velocity, inlet concentration, and boundary voltage increase, the reaction rate of the active species will be also improved.

- (3) The research directions of future work include the collaborative optimization of the electrode's microstructure, the flow field, and the flow rate to ultimately improve the local polarization uniformity. Moreover, the gas side reaction and the bubble management should also be factored into the model to further improve the battery efficiency and lifetime. And the practicability of the model should be further improved by taking into account degradation effects on the parameters.

#### CRediT authorship contribution statement

**Yansong Luo:** Methodology, Validation, Investigation, Writing – original draft, Visualization. **Wenrui Lv:** Methodology, Validation, Investigation, Visualization. **Menglian Zheng:** Conceptualization, Writing – review & editing, Funding acquisition.

#### Declaration of competing interest

The authors declare the following financial interests/personal relationships which may be considered as potential competing interests: Menglian Zheng reports that funding was provided by National Natural Science Foundation of China. Menglian Zheng reports that funding was provided by Fundamental Research Funds for the Central Universities.

#### Data availability

Data will be made available on request.

#### Acknowledgements

This work was supported by the National Natural Science Foundation of China [grant number 51606164], and the Fundamental Research Funds for the Central Universities [grant number 2022ZFJH004].

## Appendix A. Supplementary data

Supplementary data to this article can be found online at <https://doi.org/10.1016/j.est.2023.107842>.

## References

- [1] M. Zheng, J. Sun, C.J. Meinrenken, T. Wang, *Journal of Electrochemical Energy Conversion and Storage* 16 (2018).
- [2] M. Skyllas-Kazacos, M.H. Chakrabarti, S.A. Hajimolana, F.S. Mjalli, M. Saleem, *J. Electrochem. Soc.* 158 (2011) R55–R79.
- [3] A.Z. Weber, M.M. Mench, J.P. Meyers, P.N. Ross, J.T. Gostick, Q.H. Liu, *J. Appl. Electrochem.* 41 (2011) 1137–1164.
- [4] M. Gencten, Y. Sahin, *Int J Energy Res* 44 (2020) 7903–7923.
- [5] H.R. Jiang, W. Shyy, M.C. Wu, R.H. Zhang, T.S. Zhao, *Appl Energy* 233–234 (2019) 105–113.
- [6] Y. Shi, C. Eze, B. Xiong, W. He, H. Zhang, T. Lim, A. Ukil, J. Zhao, *Appl Energy* 238 (2019) 202–224.
- [7] X. Shi, O.C. Esan, X. Huo, Y. Ma, Z. Pan, L. An, T.S. Zhao, *Prog. Energy Combust. Sci.* 85 (2021), 100926.
- [8] J. Balaji, M.G. Sethuraman, S.-H. Roh, H.-Y. Jung, *Polym. Test.* 89 (2020), 106567.
- [9] M. Abdiani, E. Abouzari-Lotf, T.M. Ting, P.M. Nia, S.S. Sha'rani, A. Shockravi, A. Ahmad, *J. Power Sources* 424 (2019) 245–253.
- [10] J. Sun, M. Zheng, Z. Yang, Z. Yu, *Energy* 173 (2019) 637–646.
- [11] J. Sun, M. Zheng, Y. Luo, Z. Yu, *J. Power Sources* 428 (2019) 136–145.
- [12] M. Park, J. Ryu, W. Wang, J. Cho, *Nature Reviews Materials* 2 (2016) 1–18.
- [13] H.R. Jiang, J. Sun, L. Wei, M.C. Wu, W. Shyy, T.S. Zhao, *Energy Storage Mater* 24 (2020) 529–540.
- [14] B. Liu, M. Zheng, J. Sun, Z. Yu, *J Energy Storage* 23 (2019) 278–291.
- [15] B. Liu, M. Zheng, J. Sun, Z. Yu, *J Energy Storage* 27 (2020), 101058.
- [16] H. Al-Fetlawi, A.A. Shah, F.C. Walsh, *Electrochim. Acta* 55 (2010) 3192–3205.
- [17] A.A. Shah, H. Al-Fetlawi, F.C. Walsh, *Electrochim. Acta* 55 (2010) 1125–1139.
- [18] R. Schweiss, A. Pritzl, C. Meiser, *J. Electrochem. Soc.* 163 (2016) A2089–A2094.
- [19] S. Yao, R. Zhou, X. Huang, D. Liu, J. Cheng, *Electrochim. Acta* 374 (2021), 137895.
- [20] Y. Zeng, T. Zhao, X. Zhou, J. Zou, Y. Ren, *J. Power Sources* 352 (2017) 77–82.
- [21] I. Derr, A. Fetyan, K. Schutjajew, C. Roth, *Electrochim. Acta* 224 (2017) 9–16.
- [22] A.A. Wong, S.M. Rubinstein, M.J. Aziz, *Cell Rep Phys Sci* 2 (2021).
- [23] L. Wei, T.S. Zhao, Q. Xu, X.L. Zhou, Z.H. Zhang, *Appl Energy* 190 (2017) 1112–1118.
- [24] J.K. Mo, Z.Y. Kang, G.Q. Yang, Y.F. Li, S.T. Retterer, D.A. Cullen, T.J. Toops, G. Bender, B.S. Pivovar, J.B. Green, F.Y. Zhang, *J. Mater. Chem. A* 5 (2017) 18469–18475.
- [25] L. Chen, A. He, J. Zhao, Q. Kang, Z.-Y. Li, J. Carmeliet, N. Shikazono, W.-Q. Tao, *Prog. Energy Combust. Sci.* 88 (2022), 100968.
- [26] G. Qiu, C.R. Dennison, K.W. Knehr, E.C. Kumbur, Y. Sun, *J. Power Sources* 219 (2012) 223–234.
- [27] G. Qiu, A.S. Joshi, C.R. Dennison, K.W. Knehr, E.C. Kumbur, Y. Sun, *Electrochim. Acta* 64 (2012) 46–64.
- [28] D. Maggolino, F. Zanini, F. Picano, A. Trovo, S. Carmignato, M. Guarnieri, *Energy Storage Mater* 16 (2019) 91–96.
- [29] D. Zhang, A. Forner-Cuenca, O.O. Taiwo, V. Yufit, F.R. Brushett, N.P. Brandon, S. Gu, Q. Cai, *J. Power Sources* 447 (2020), 227249.
- [30] L.S. Xiao, M.J. Luo, L.J. Zhu, K.J. Duan, N. Bevilacqua, L. Eifert, R. Zeis, P.C. Sui, *J. Electrochem. Soc.* 167 (2020).
- [31] L. Chen, Y. He, W.-Q. Tao, P. Zelenay, R. Mukundan, Q. Kang, *Electrochim. Acta* 248 (2017) 425–439.
- [32] M.A. Sadeghi, M. Aghighi, J. Barralet, J.T. Gostick, *Chem. Eng. J.* 330 (2017) 1002–1011.
- [33] A.G. Lombardo, B.A. Simon, O. Taiwo, S.J. Neethling, N.P. Brandon, *J Energy Storage* 24 (2019).
- [34] T. Li, F. Xing, T. Liu, J. Sun, D. Shi, H. Zhang, X. Li, *Energy Environmental Science* 13 (2020) 4353–4361.
- [35] S. Wan, X. Liang, H. Jiang, J. Sun, N. Djilali, T. Zhao, *Appl Energy* 298 (2021), 117177.
- [36] S. Wan, H. Jiang, Z. Guo, C. He, X. Liang, N. Djilali, T. Zhao, *Energy Environmental Science* 15 (2022) 2874–2888.
- [37] J. Bao, V. Murugesan, C.J. Kamp, Y.Y. Shao, L.T. Yan, W. Wang, *Adv Theor Simul* 3 (2020).
- [38] S. Wan, X. Liang, H.M. Zhang, C.X. Sun, Y. Zou, T. Zhang, *J. Power Sources* 203 (2012) 153–158.
- [39] C.Y. Ling, H. Cao, M.L. Chng, M. Han, E. Birgersson, *J. Power Sources* 294 (2015) 305–311.
- [40] D.K. Kim, S.J. Yoon, J. Lee, S. Kim, *Appl Energy* 228 (2018) 891–901.
- [41] A. Tang, J. Bao, M. Skyllas-Kazacos, *J. Power Sources* 248 (2014) 154–162.
- [42] S. König, M.R. Suriyah, T. Leibfried, *J. Power Sources* 333 (2016) 134–144.
- [43] J. Fu, M. Zheng, X. Wang, J. Sun, T. Wang, *Journal of Energy Engineering* 143 (2017) 04017064.
- [44] T. Wang, J.H. Fu, M.L. Zheng, Z.T. Yu, *Appl Energy* 227 (2018) 613–623.
- [45] W. Xiao, L. Tan, *Renew. Energy* 133 (2019) 1445–1454.
- [46] W.W. Yang, X.S. Bai, W.Y. Zhang, M.Y. Lu, Q. Xu, *J. Power Sources* 457 (2020), 228002.
- [47] Q. He, Y. Fu, P. Stinis, A. Tartakovsky, *J. Power Sources* 542 (2022), 231807.
- [48] D. You, H. Zhang, J. Chen, *Electrochim. Acta* 54 (2009) 6827–6836.
- [49] F. Li, Y. Wei, P. Tan, Y. Zeng, Y. Yuan, *J Energy Storage* 32 (2020), 101781.
- [50] X.-G. Yang, Q. Ye, P. Cheng, T.S. Zhao, *Appl Energy* 145 (2015) 306–319.
- [51] X.L. Zhou, T.S. Zhao, L. An, Y.K. Zeng, X.H. Yan, *Appl Energy* 158 (2015) 157–166.
- [52] F. Yang, D. Qu, Y. Chai, M. Zhu, L. Fan, *Int J Hydrogen Energy* 47 (2022) 27358–27373.
- [53] M.-Y. Lu, Y.-H. Jiao, X.-Y. Tang, W.-W. Yang, M. Ye, Q. Xu, *J Energy Storage* 35 (2021), 102284.
- [54] C. Yin, Y. Gao, G. Xie, T. Li, H. Tang, *J. Power Sources* 438 (2019), 227023.
- [55] Y. Kim, Y.Y. Choi, N. Yun, M. Yang, Y. Jeon, K.J. Kim, J.-I. Choi, *J. Power Sources* 408 (2018) 128–135.
- [56] X.K. Ma, H.M. Zhang, F. Xing, *Electrochim. Acta* 58 (2011) 238–246.
- [57] M.A. Sadeghi, M. Aganou, M. Kok, M. Aghighi, G. Merle, J. Barralet, J. Gostick, *J. Electrochem. Soc.* 166 (2019) A2121–A2130.
- [58] B. Xiong, Y. Li, Y. Ding, J. Wang, Z. Wei, J. Zhao, X. Ai, J. Fang, *J. Power Sources* 564 (2023), 232814.
- [59] I.V. Zenyuk, D.Y. Parkinson, L.G. Connolly, A.Z. Weber, *J. Power Sources* 328 (2016) 364–376.
- [60] D. Emmel, J.D. Hofmann, T. Arlt, I. Manke, G.D. Wehinger, D. Schröder, *Acs Appl Energy Mater* 3 (2020) 4384–4393.